

Effects of Dust Coagulation on Streaming Instability

KA WAI HO,^{1,2} HUI LI,¹ AND SHENGTAI LI¹

¹*Theoretical Division, Los Alamos National Laboratory*

²*Department of Astronomy, University of Wisconsin-Madison*

ABSTRACT

Streaming Instability (SI) in dust has long been thought to be a promising process in triggering planetesimal formation in the protoplanetary disks (PPDs). In this study, we present the first numerical investigation that models the SI in the vertically stratified disk together with the dust coagulation process. Our simulations reveal that, even with the initial small dust sizes, because dust coagulation promotes dust size growth, SI can eventually still be triggered. Specifically, dust coagulation, limited only by dust fragmentation, broadens the parameter boundaries obtained from previous SI studies using single dust species. We describe the various stages of dust dynamics along with their size evolution, and explore the impact of different dust fragmentation velocities. Implications of these results for realistic PPDs are also discussed.

Keywords: Planet formation (1241); Protoplanetary disks (1300); Planetesimals (1259); Hydrodynamics (1963); Hydrodynamical simulations (767); Gas-to-dust ratio (638)

1. INTRODUCTION

The growth of micron-sized dust to kilometer-sized planetesimals is a key stage of the planet formation in PPDs. Various processes contribute to the overall evolution, including dust size growth and self-gravitational collapse of dust clumps. The latter process is expected to occur when the concentrated dust clump density exceeds the critical Roche density. Several instability mechanisms have been proposed to account for the accumulation stage of the dust clumps to trigger the self-gravitational collapse (National Academies of Sciences, Engineering, and Medicine 2022), with the Streaming Instability (SI) being a prime candidate (Youdin & Goodman 2005).

Extensive analytical and numerical studies have explored the conditions under which SI triggers the formation of sufficiently dense clumps to surpass the local Roche density (e.g., Johansen & Youdin 2007; Kowalik et al. 2013; Armitage et al. 2016). These studies have established constraints on three critical parameters that control the clumping process: the normalized stopping time (τ_s), a measure of dust particle coupling to the gas; the dust-to-gas (D/G) ratio; and the turbulent intensity (Umurhan et al. 2020; Chen & Lin 2020; Li & Youdin 2021). These parameters collectively determine the conditions required for robust clumping. Recent investigations (largely axisymmetric) by Li & Youdin (2021) have revealed that clumping can occur at even smaller particle sizes and lower D/G ratios than previously thought. Their findings show that clumping can arise with D/G ratios as

low as 0.003 for optimally-sized dust particles, or with τ_s as small as 10^{-3} for higher D/G ratios. These results were obtained from extended simulations spanning 500 Keplerian orbits, crucial for allowing the onset of strong SI clumping to fully develop across diverse parameters with effectively weak values of self-generated turbulence. Moreover, it remains uncertain whether the particle clumping behavior observed in 3D simulations is consistent with the results from axisymmetric studies

Most of these previous studies have used a single dust size (or a single τ_s). In realistic PPDs, however, dust tends to have a size distribution along with dust coagulation and fragmentation processes (e.g., Birnstiel et al. 2010; Li et al. 2019; Drażkowska et al. 2019; Laune et al. 2020; Li et al. 2020). The dust size evolution opens up the possibility that the SI can eventually get triggered in dusty environment where the initial dust sizes are relatively small (or τ_s below the traditional SI threshold). In addition, there could be interplay between the evolution of SI and the dust sizes, potentially altering SI dynamics and impacting dense clump formation, as well as altering the dust size distribution and affecting the growth of larger particles. This is a topic of great interest (e.g., Drażkowska & Dullemond 2014; Schaffer et al. 2018; McNally et al. 2021; Tominaga & Tanaka 2023), but due to the expensive computational cost of resolving the coagulation at high resolution for extended long duration, most of the previous studies have focused on either analytical approach or simulations with a limited number of dust species that omit coagulation (Schaffer et al. 2018; Zhu & Yang 2021; Rucsa & Wadsley 2023). However, recent advancements in numerical simulations, particularly the mesh refinement capabilities, significantly reduce the computational cost while maintain-

ing the high resolution necessary to resolve the SI dynamics at the disk midplane.

In this paper, we present some of the first numerical simulations incorporating both dust size evolution and the SI, aiming to explore one key question: how the dust size evolution will affect the SI. Our paper is structured as follows: Section 2 describes our numerical scheme, Section 3 presents our results, Section 4 discusses their implications, and Section 5 summarizes our findings.

2. METHODS

2.1. Hydrodynamical Modelling

To simulate the coupled dynamics of gas and dust within a PPD, we employ the *Athena++* magnetohydrodynamic (MHD) code augmented with its integrated multi-fluid dust module. This configuration allows for the simultaneous evolution of both gas and dust species (Stone et al. 2020; Huang & Bai 2022). An important distinction is that we have implemented a new multi-fluid approach for dust modeling along with dust coagulation dynamics in *Athena++*. To model dust coagulation and fragmentation, we adopt the implementation described in another code called LA-COMPASS (Li et al. 2019; Drazkowska et al. 2019; Laune et al. 2020; Li et al. 2020), which has a dust coagulation module using an explicit integration scheme to solve the Smoluchowski equation Brauer et al. (2008). This model incorporates turbulent mixing and Brownian motion as sources of collision velocities. To manage the high computational cost associated with solving the dust coagulation equations, we implement a sub-stepping routine. The dust coagulation module is called every $\Delta t = 0.1/\Omega$ of the simulation, with Ω being the Keplerian frequency at radius r , ensuring a balance between computational efficiency and accuracy in the coagulation calculations. We employ a first-order implicit method for drag modeling in conjunction with a second-order piecewise linear method to accurately model the dynamic interactions between gas and dust. (The details of this new module in *Athena++* will be presented in a future publication.)

Table 1. 2D Simulation Parameters with Coagulation

Runs	$\tau_{s,0}$	τ_s ranges	N_{dust}	v_f/c_s	Ωt_{sim}
run1	10^{-2}	$[7.36 \times 10^{-6}, 0.736]$	101	2.5×10^{-3}	2200
run2	10^{-2}	$[7.36 \times 10^{-5}, 7.36]$	101	5.0×10^{-3}	2200
run3	10^{-2}	$[2.58 \times 10^{-3}, 25.8]$	81	2.5×10^{-2}	2200
run4	10^{-3}	$[2.58 \times 10^{-4}, 2.58]$	81	2.5×10^{-2}	3000

2.2. Dust Evolution Modelling

For dust, we assume it is in the Epstein’s regime, so that Stokes Number $St = (\rho_p a v_K)/(\rho_g r c_s) \approx (a \rho_p)/\Sigma_g$, where ρ_p is the dust internal density (taken to be 1.25 g/cm^3), a is dust size, c_s is the gas sound speed and v_K is the gas Keplerian speed at radius r . The disk scale height $H = r c_s/v_K$.

The gas density is ρ_g and its surface density is $\Sigma_g = \rho_g H$. Note that the variations in gas density during the simulations are very small. The stopping time t_s is normalized as $\tau_s = t_s \Omega = St$. A key remaining parameter is the fragmentation velocity v_f . Due to its high variability and dependence on environmental factors like the presence of water ice, we investigate cases with $v_f/c_s = 2.5 \times 10^{-3}, 5 \times 10^{-3}$, and 2.5×10^{-2} to explore how this parameter influences the SI.

To study the effects of dust coagulation on the SI, we follow the previous approach in numerical studies of the SI by utilizing a local shearing box approximation to model a vertically stratified patch of the PPD without self-gravity. Our physical setup and boundary conditions directly follow those defined in Li & Youdin (2021). The setup employs a two-dimensional $x - z$ shearing box with the standard shearing periodic boundary conditions in x , and the outflow boundary condition in z . The simulation box has $L_x \times L_z = 0.8H \times 0.4H$, which has a base resolution of 240×480 . Furthermore, to reduce the computational cost, we introduce a specific mesh refinement at the midplane between $z = \pm 0.05H$. This region has a resolution of 1920×3840 which is eight times higher than regions at higher disk heights. This will help capture most of the relevant dynamics occurring at the midplane, and it ensures that the resolution requirements proposed by Li & Youdin (2021) will be met.

Table 1 lists the simulation parameters. For all these runs, the initial total dust to gas density ratio is set to be $D/G = 0.015$, which is to match the desired value from Li & Youdin (2021), for which the SI is not excited.

For the initial dust size distribution, the dust at midplane initially has $\tau_{s,0} = 10^{-2}$ or 10^{-3} (see Table 1). To capture the dust size evolution across a wide range, we use either 81 or 101 logarithmic dust size bins, spanning four to five orders of magnitude in stopping time (see Table 1), ensuring a comprehensive representation of the dust population.

To put these dimensionless parameters in perspective, we can use a minimum mass solar nebula model density profile located at 10 AU, $\Sigma_g \sim 53.3 \text{ g/cm}^2$ and $c_s = 0.4 \text{ km/s}$ or $c_s/v_K = 0.04$. From these, we can find the gas density $\rho_g \approx 8.88 \times 10^{-12} \text{ g/cm}^3$ and the Roche density is $\sim 5 \times 10^{-10} \text{ g/cm}^3$, which is $\sim 56 \times$ the gas density. To study the interplay between vertical settling and dust coagulation effect, we set the initial dust height $H_d = 0.09H$. The turbulence would be developed due to the excitation of SI, and no external sources of turbulence have been implemented. The fragmentation velocity to sound speed ratio $v_f/c_s = 2.5, 5$, and 25×10^{-3} will give values of v_f as 1, 2, and 10 m/s, respectively. The initial dust size is 0.43 cm for $\tau_{s,0} = 10^{-2}$. For all the simulations, We have used a parameter $\alpha_{coag} = 10^{-5}$ in the coagulation model to mimic the turbulence expected from SI. Furthermore, the dust sizes captured in simulations can vary between $\sim 3 \mu\text{m}$ to 30 cm for $\tau_s = 7.36 \times 10^{-6}$ to 0.736.

For the computational cost, each simulation takes 5040 cores and ran for 2 to 4 days in NERSC Perlmutter or LANL

Chicoma cluster, with an estimated cost of 200k to 300k CPU hours per run.

3. RESULTS

3.1. Dust coagulation & SI

In the classical SI scenario, the development of SI can be divided into four stages: vertical settling, pre-clumping, strong clumping, and post-clumping phase. In the settling phase, dust particles vertically settle from higher latitudes to the mid-plane, resulting in an enhancement of mid-plane dust density. This is followed by the pre-clumping phase, a transition phase before strong clumping with a weak increase of mid-density density. In the strong clumping stage, it shows the excitation of SI with dust concentrations rapidly growing and merging into larger and denser clumps. Finally, in the post-clumping stage, the largest dust aggregates that have reached Roche density decouple from the gas and have the potential to evolve into planetesimals through gravitational collapse. In this study, we will follow a similar classification scheme to better understand how dust coagulation makes an impact on the various stage of SI.

We emphasize that we have used an initial $D/G = 0.015$ for all the runs presented in this paper, which was shown not to excite SI in the single dust size study with $\tau_s \leq 10^{-2}$ by Li & Youdin (2021). We use this initial state to highlight how dust coagulation could affect the overall evolution of dust clumping and whether SI can be excited after all. The basic idea is relatively straightforward: with coagulation, the dust size growth will increase their τ_s , enhancing the coupling between dust and gas, and potentially leading to SI.

3.1.1. $\tau_{s,0} = 10^{-2}$ Cases

Fig. 1 provides the evolution of the maximum dust clump density and the density-weighted averages of τ_s at the mid-plane region for all three runs with $\tau_{s,0} = 10^{-2}$ (see Table 1). It is evident that, in terms of the dust density evolution, all runs reach quite high maximum dust density up to a thousand times the gas density, a clear sign of the SI. This outcome, which is different from the previous single fixed dust size simulation, is presumably solely caused by the dust size growth and is the key result of this paper.

Similar to the previous single sized SI studies, these runs show approximately four stages: First, before $t < 300\Omega^{-1}$, the dust vertically settles towards the mid-plane during the “settling phase”. Second, the dust transitions into the “pre-clumping phase” up to $t \sim 800\Omega^{-1}$, with a relatively mild growth of the peak dust density by a factor of two. Third, after $t > 800\Omega^{-1}$, the dust enters the “strong clumping phase”, rather quickly for run2 and run3 though a bit slower for run1. The $\rho_{dust,max}$ grows quite robustly by another factory of up to $\sim 10^2$ for run2 and run3, and shows a weaker growth by another large factor of ~ 4 for run1. This implies that the peak dust density will exceed the Roche density for run2 and approximately for run3, but is still below it for run1. Finally, after these rigorous growth stages, all three runs transition into a “quasi-equilibrium” stage between $1250\Omega^{-1}$ and

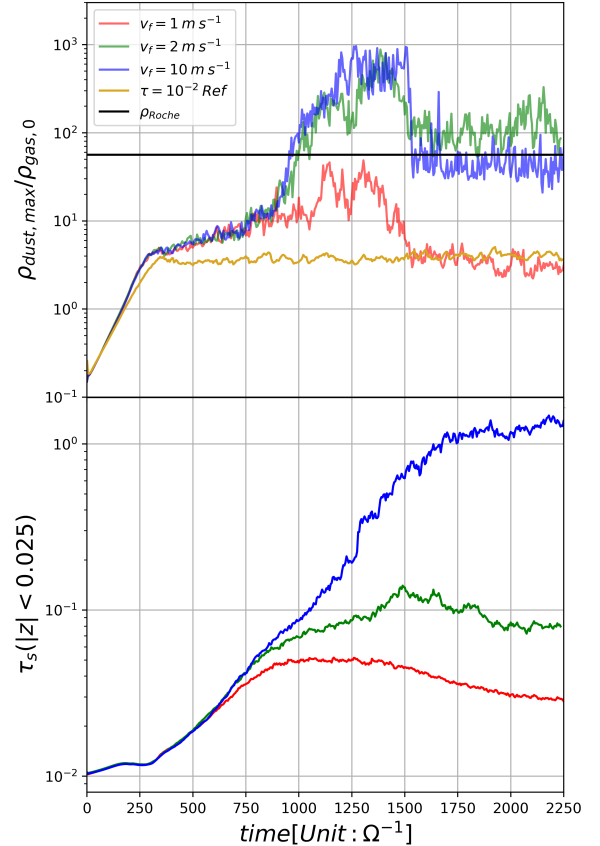


Figure 1. Temporal evolution of the mid-plane maximum dust density (top) and the mass-averaged normalized stopping time (bottom) in simulations with the initial stopping time $\tau_{s,0} = 10^{-2}$ (the first three runs in Table 1). We adopt $c_s = 0.4$ km/s in all these runs. The result from a single dust size run with $\tau_{s,0} = 10^{-2}$ without coagulation is also shown for reference (yellow lines).

$1500\Omega^{-1}$, with a relatively steady maximum dust density. The final maximum dust density remains at several times the gas density for run1, and ~ 100 times the gas density for run2 and 3.

Along with the dust clumping and density growth, the dust size also grows in a corresponding fashion as shown in the bottom panel of Fig.1 where the density-weighted dust size within $z \pm 0.025$ is calculated. While the dust size growth is rather modest during the settling stage, all three runs show similar amount of growth during the pre-clumping phase, up to size $\tau_s \sim 0.4 - 0.6$. As the SI is excited and strong clumping ensues, the growth during the strong clumping phase is different for three runs, with higher fragmentation velocities reaching much larger dust sizes. For example, run1 with the lowest v_f shows a saturated dust size at $\tau_s \sim 0.05$, whereas run2 produces $\tau_s \sim 0.1$ and runs grows to $\tau_s \sim 0.8$. During the final equilibrium stage, the final τ_s for run1-3 settles at 0.03, 0.08, and 1.5, respectively.

It seems that the coagulation does not lead to any visible differences among the three runs up to $t \sim 700\Omega^{-1}$ but substantial differences emerge after that. This is consistent with

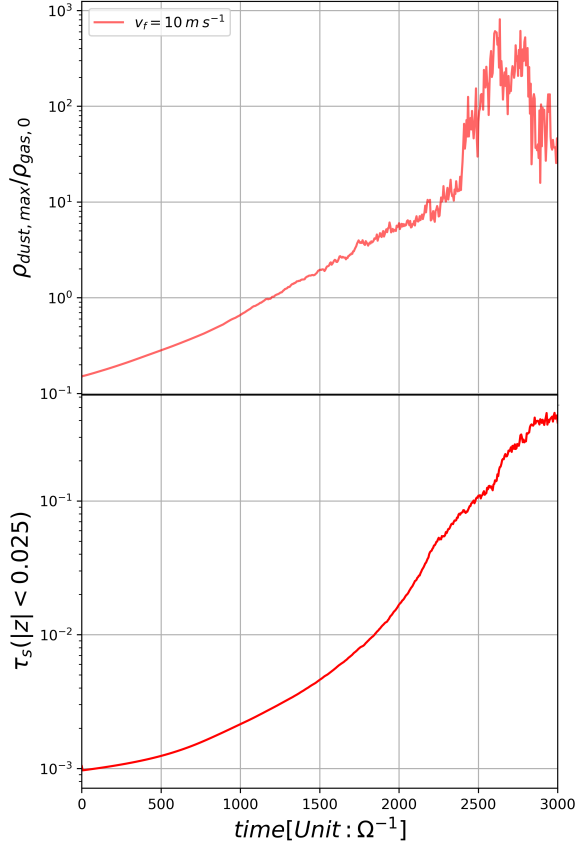


Figure 2. Temporal evolution for $\tau_{s,0} = 10^{-3}$ case.

the expectation that, as higher density dust clumps develop due to SI, the coagulation process inside the dense clumps will alter the dust size distribution significantly.

The result of a single sized dust $\tau_{s,0} = 10^{-2}$ without coagulation is also shown in the top panel of Fig. 1. As discussed earlier, this case does not produce SI (Li & Youdin 2021), so the final dust density (though showing increase due to the vertical settling) remains relatively low. This further supports the main conclusion that the coagulation is essential in triggering the SI.

3.1.2. $\tau_{s,0} = 10^{-3}$ Case

Fig. 2 illustrates the evolution for $\tau_{s,0} = 10^{-3}$ and $v_f/c_s = 2.5 \times 10^{-2}$. In contrast to the $\tau_{s,0} = 10^{-2}$ cases, run 4 demonstrates distinctive behavior during the vertical settling and pre-clumping phases. Because of the small initial τ_s , the vertical settling phase takes a lot longer, extending to $t \approx 2000\Omega^{-1}$. Unlike the limited dust growth observed in $\tau_{s,0} = 10^{-2}$ cases, the dust size growth in this case is by a factor of 20 during the settling phase. We also notice a slight dust density fluctuation starting at $t = 1500\Omega^{-1}$, potentially indicating that some kind of instability in the dust may have already begun at this stage of the vertical settling phase. The system then transitions to the pre-clumping phase between $t = 2000$ and $2300\Omega^{-1}$. The duration of the pre-clumping phase is also shorter compared to run 3. It continues until

the average dust size reaches about 0.08, at which point the system undergoes an instability, leading to a strong clumping phase with the peak density reaching $\sim 900\rho_{g,0}$. Following this transition, the system’s evolutionary trajectory closely aligns with that observed in run 3 with SI being excited. Given its high v_f , the final τ_s is relatively large, reaching ~ 0.4 .

3.2. Mid-Plane Morphology of Dust Distribution

To understand the consequence of coagulation on SI in more detail, Figure 3 displays snapshots of the dust density and mass-averaged stopping time, roughly $100\Omega^{-1}$ after the strong clumping phase has started for run1-3 individually.

All cases reveal the formation of dense dust clumps with turbulent structures from SI (the left panel of Fig. 3). As the fragmentation velocity gets larger, several trends are visible. With higher v_f , dust is expected to grow to larger sizes, which is seen (the right panel of Fig. 3). In turn, higher τ_s dust leads to a more spatially settled dust distribution towards the mid-plane. As more dust concentrates at the midplane, numerous highly concentrated dust clumps form. The highest density clumps also promote higher τ_s as well.

3.3. Evolution of Dust Size Distribution

Figure 4 presents the joint evolution of dust density and size (the top three rows) and the overall mass-weighted size evolution (the bottom row), for run 1-3 with different fragmentation velocities. We emphasize that, for each of these runs, adequate dust size bins are used to allow the dust size growth, as given in Table 1. For all cases, by the end of the settling phase $\Omega t \sim 300 - 400$, there is only a modest dust size growth by a factor of ~ 2 . By the end of pre-clumping phase at $\Omega t \sim 800$ (bottom row), the dust size distribution has now undergone significant coagulation and shifts its peak from the initial $\tau_s = 0.01$ to $\tau_s \sim 0.06$. The similarity of dust size distributions for these three cases at this time is consistent with the conclusions from Fig. 1 that the settling is faster than coagulation for these runs and the coagulation mostly occur at the mid-plane when the dust has settled.

At $\Omega t = 1200$ and 2000 , which correspond to the peak and saturation of SI respectively, different v_f values make a marked difference. For $v_f = 1$ m/s, the dust size distribution maintains its peak at $\tau_s \sim 0.06$ and the SI is visible but weak, producing relatively fewer dense dust clumps (cf. Fig. 3). For $v_f = 2$ m/s, the peak gradually increases beyond $\tau_s \sim 0.1$, and shows signatures for a two-peak distribution at $\tau_s \sim 0.08 - 0.1$ and $\tau_s \sim 0.3 - 0.5$, respectively. When combining with the spatial distributions shown in Fig. 1, it is suggestive that the average dust size inside the densest clumps corresponds to the higher τ_s peak. For 10 m/s, the dust size distributions eventually exhibit two peaks: one at $\tau_s \sim 0.1$ and the other at $\tau_s \sim 2 - 4$. We can see that the dust with $\tau_s \sim 2 - 4$ is concentrated in a very narrow layer at the mid-plane along with the highest density clumps, whereas dust with $\tau_s \sim 0.1$ occupies around the midplane with a wider extent. Evidently, for dust inside the dense clumps (due to SI),

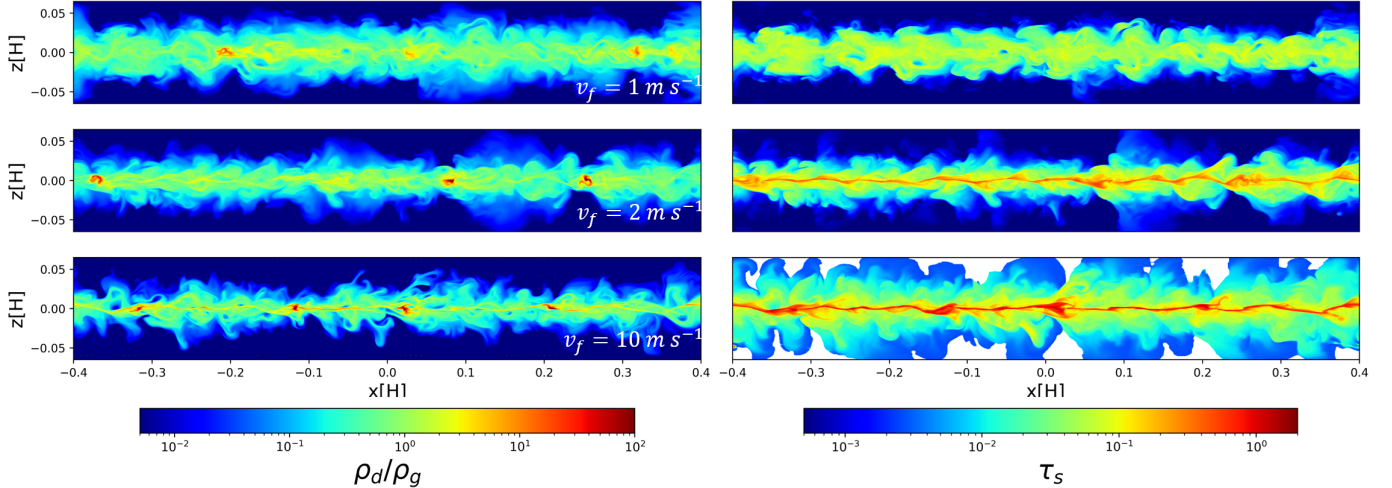


Figure 3. Spatial distribution of dust density ratio ρ_d/ρ_g (left) and the mass-averaged stopping time τ_s (right) for varying fragmentation velocities $v_f = 1, 2,$ and 10 m/s . (White region indicates local dust density falling below $10^{-8}\rho_g$ and the mass averaged statistics not computed.) Each frame is chosen to be $\sim 100\Omega^{-1}$ after the strong clumping phase has started for run1-3 respectively (cf. Fig. 1), which are $t = 1300\Omega^{-1}$ (run 1), and $1350\Omega^{-1}$ (run 2 and 3).

coagulation further pushes their sizes to $\tau_s = 2 - 4$; for those dust that stay outside clumps, their size (due to coagulation and fragmentation) is balanced at $\tau_s \approx 0.1$. This eventually leads to the two dust size populations. It is clear that larger v_f promotes more dust grows into the larger sizes and form a large number of clumps as well.

4. DISCUSSION

Relaxation of the Streaming Instability Threshold and the impact of coagulation in SI development. Previous studies have found that the initiation of SI is contingent upon a specific range for both the average particle size and the mass ratio, which facilitates the mass accumulation of dust clumps. For example, for disks with a low mass ratio ($D/G < 0.02$), effective SI occurs within a particle size range of $\tau = 2 \times 10^{-2}$ to $\tau = 1$ (Li & Youdin 2021). A higher mass ratio enables smaller dust sizes to trigger SI. Our study demonstrates that the process of dust coagulation significantly influences the SI dynamics. Notably, even for initial conditions with $\langle \tau_0 \rangle = 10^{-3}$, coagulation could increase the dust size by an order of magnitude within a few hundred orbits, thereby triggering the SI. This finding relaxes the more stringent particle size requirements previously identified (see Fig. 1 in Li & Youdin (2021)). Due to the effect of dust coagulation, regions previously identified as SI-inactive could evolve into SI-active regimes within the timescale of SI evolution.

Additionally, we observed differences in the evolution of SI between small and large initial dust size distributions. This is illustrated by comparing run 3 ($\tau_{s,0} = 10^{-2}$) and run 4 ($\tau_{s,0} = 10^{-3}$). The settling timescale can be estimated as $\tau_{set} \propto 1/\tau_{s,0}$ (Laibe et al. 2014) and the coagulation timescale is $\tau_{coag} \propto \tau_{s,0}$ (Tominaga & Tanaka 2023), assuming perfect sticking. On the one hand, for small τ_s , the coagulation timescale can be much shorter than the settling

timescale, so the dust undergoes appreciable size growth during the settling process. On the other hand, it will take longer time for the initial small dust to grow to a certain value of τ_s where SI can be triggered. The evolution trajectory shown in Fig. 2 indicates such dynamics.

Importance of the Fragmentation Velocity. Our results indicate that the fragmentation velocity, v_f , is a critical factor in the dust growth process during the clumping phase. It influences both the peak dust-to-gas ratio and the resultant average dust size. In scenarios where v_f is low (e.g., $v_f = 1 \text{ m/s}$), the coagulation process tends to be less efficient, which may kill the streaming instability during the strong clumping phase. Conversely, our findings show that a higher fragmentation velocity can promote both dust size growth and effective dust clump formation.

Conditions in Protoplanetary Disks. The synergistic efficacy of SI and dust coagulation, as we have discussed, hinges on an extended time frame and a higher fragmentation velocity. A significant concern, however, is the radial drift of larger dust particles. Over the timescale of hundreds of orbits, this drift can lead to the inward drift of large dust grains, which is not completely captured in shearing box simulations. Moreover, the higher fragmentation velocity suggests a preferential composition of dust grains – icy grains rather than silicates are advantageous. These conditions are likely to be found near the snow line, where the back-reaction effect can play a significant role (Garate et al. 2020). The snow line could act as a pressure bump, impeding the inward drift of dust and potentially creating a higher local dust-to-gas ratio region. Although the pressure bump effect of the snow line may not favor single-species SI for planetesimal formation in millimeter grain scenario (Carrera & Simon 2022), the presence of icy grains may elevate the fragmentation velocity threshold to 10 m/s , compared to the typical 1 m/s for silicate grains. This increase in fragmentation velocity promotes

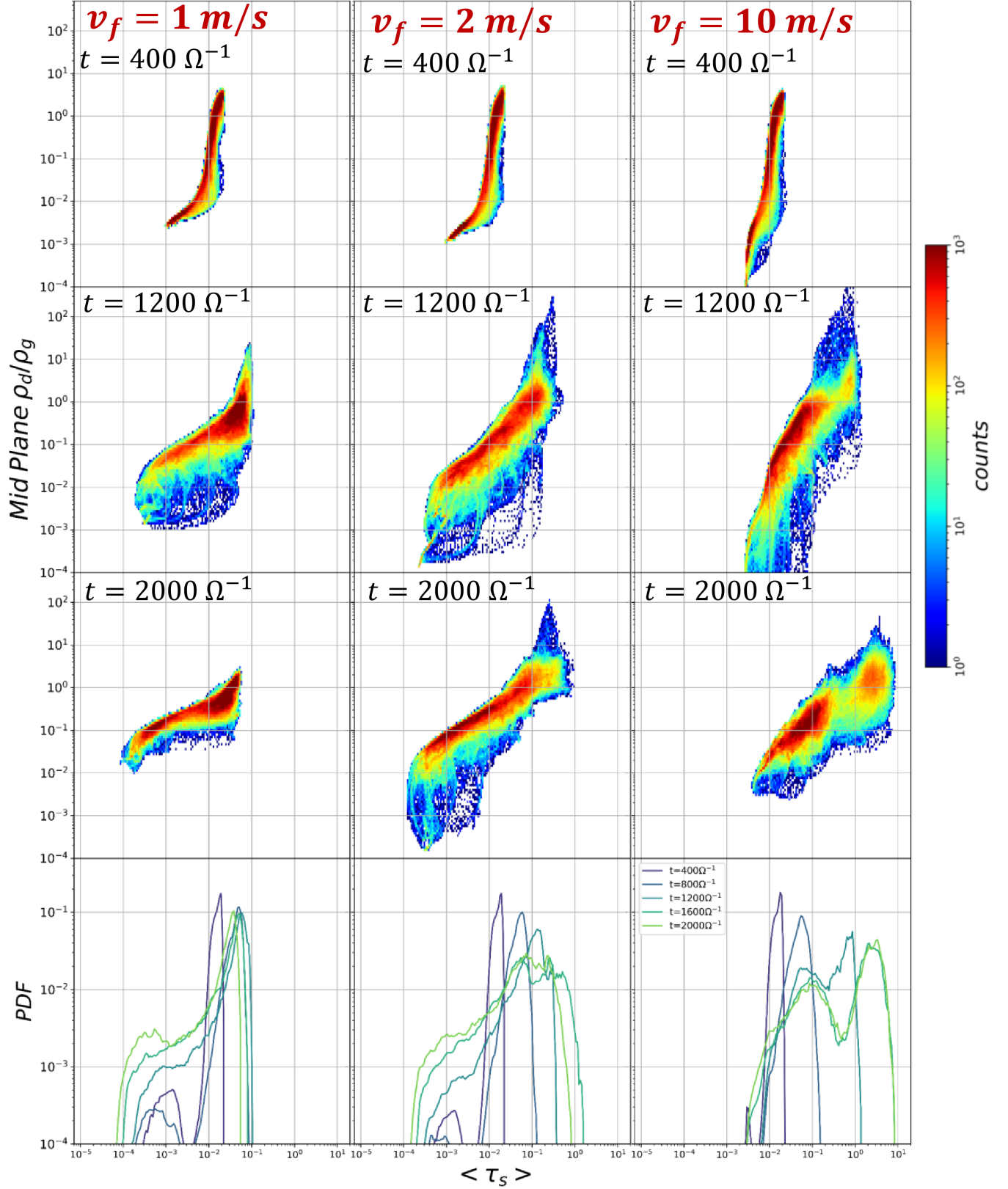


Figure 4. Temporal Evolution of the mid-plane ($|z| < 0.05H$) dust density ρ_d/ρ_g and its mass-weighted size $\langle \tau_s \rangle$ for run 1-3 with three fragmentation velocities of 1 m/s (left column), 2 m/s (middle), and 10 m/s (right), respectively. The bottom row is the evolution of the probability density function of dust size distribution for run 1-3, respectively. All runs have an initial stopping time $\tau_{s,0} = 10^{-2}$ and initial $\rho_d/\rho_g = 1.5 \times 10^{-2}$.

dust coagulation and growth, thereby sustaining SI during the strong clumping phase. Our studies has not included the effects of self-gravity, which is expected to play a role particularly in the dense dust clumps. Such effects will be explored in future studies.

Vertical Diffusion and Turbulence There is the self-generated turbulence from SI, helping the vertical diffusion of gas and dust. The vertical diffusion can be estimated using $D_{p,z} = H_p^2 \Omega \tau_s$, or $\alpha_{diff} = D_p / (c_s H)$ where H is the gas scale height, H_p is the mass-averaged dust scale height with $H \gg H_p$, and τ_s is the mass-averaged dust dimensionless stopping time, respectively (Dubrulle et al. 1995; Youdin 2010). We evaluated the spatial and temporal evolution of α_{diff} for runs with initial $\tau_{s,0} = 10^{-2}$. We find that the average α_{diff} at the mid-plane reaches $\sim 10^{-5}$ during the nonlinear saturated stage of SI for both Run 1 and 2. For the highest $v_f = 10m/s$ case (Run 3), the final $\alpha_{diff} \sim 10^{-4}$ as τ_s approaches 1. These estimates are also consistent with our analysis of Reynolds stresses using the actual gas velocity fluctuations in three components (Balbus & Hawley 1998; Baronett et al. 2022). Generally the α_{diff} obtained in our study is consistent with the findings of Umurhan et al. (2020); Li & Youdin (2021). However, as noted by Sengupta & Umurhan (2023), the turbulence statistics of axis-symmetric simulations used in this study may differ from those in 3D simulations. Future studies using 3D simulations are needed.

In order to make direct comparisons with the previous non-coagulation studies of SI which did not include an explicit viscous processes in the hydrodynamics of gas and dust, we opt not to include explicit viscosity in the hydrodynamics as well. As for the effects of turbulence on coagulation, a larger α_{coaag} is expected to modify dust evolution significantly, as it would enhance the collision rate in the Smoluchowski equation. Consequently, stronger turbulence would lead to more rapid dust growth. However, the increased relative velocities associated with stronger turbulence would also impose a fragmentation barrier, limiting the maximum dust size that can be achieved. Future studies incorporating realistic α_{coaag} values in multi-dimensional simulations are needed to better capture dust evolution under the influence of hydrodynamical motion.

The Bouncing Barrier and Its Impact on SI The results presented here consider a dust coagulation model (Brauer et al. 2008), accounting for the coagulation and fragmentation of dust grains. However, another important process in dust evolution, namely the bouncing physics, has not been included (e.g., Wurm & Teiser 2021). The bouncing barrier, where particles become less likely to stick together and instead tend to bounce off each other, could significantly alter the dust size distribution and, consequently, the dynamics of SI. Previous studies on dust evolution models incorporating bouncing physics have primarily been conducted in one-dimensional simulations (e.g., Estrada et al. 2016, 2022; Yap & Batygin 2024; Dominik & Dullemond 2024). These studies suggest that the bouncing barrier can lead to a very narrow, size distribution, removing both large and μm -sized grains in the process, with most dust particles growing and stabilizing at ap-

proximately 10^{-2} cm (Dominik & Dullemond 2024). It is currently unknown on how the inclusion of bouncing physics in our model will alter the outcomes presented in this paper. If it leads to a more concentrated size distribution, it is conceivable that the effects of dust size growth on the SI development will be reduced as well. However, it is important to note that dust evolution behavior can differ significantly in higher-dimensional simulations. This has been demonstrated for traditional dust coagulation models, where larger dust formation is more favored in 2D/3D settings (Li et al. 2019; Drażkowska et al. 2019; Laune et al. 2020; Li et al. 2020) compare to the 1D (Birnstiel et al. 2012). Given these dimensional dependencies, the impact of the bouncing barrier on SI in multi-dimensional scenarios remains an open question, and the future multi dimensional simulations incorporating bouncing physics are needed.

While our current study does not include bouncing effects, it offers insights into certain aspects of particle growth and streaming instability under idealized conditions, providing a baseline for comparison with more complex models in future.

5. CONCLUSIONS

In this study, we have numerically explored the synergy between streaming instability and dust coagulation, specifically examining the strong particle clumping effect in the absence of self-gravity. Our findings emphasize the potential of dust size growth through coagulation to facilitate further the excitation and growth of SI. Our principal conclusions are:

1. Within the timescale of a few hundred orbits, the dust coagulation could potentially grow the average dust size by a factor of several up to two orders of magnitudes, producing dust into $\tau_s \sim 0.1 - 1$ range, satisfying the condition for triggering SI. This extends the traditional boundary for exciting SI to even broader disk conditions.
2. The fragmentation velocity plays a role in regulating the dust size distribution in dense dust clumps and their surrounding regions. Consequently, it also affects the strength and final outcome of SI.

Numerical studies of the combined effects of the initial dust size, dust settling, coagulation, and SI are beginning to provide a more comprehensive picture of the dynamics in PPDs. Future studies including the effects of dust bouncing, snow lines and self-gravity will be crucial for understanding the planetesimal formation.

ACKNOWLEDGMENTS

We acknowledge Mordecai-Mark Mac Low and Kratter Kaitlin for fruitful discussions during the final stage of the paper. We would also like to thank the referee for many useful comments and suggestions which significantly improved this work. We thank Michael Halfmoon for granting additional NERSC time needed for this project. Support

by the LANL/LDRD program is gratefully acknowledged. This research used resources provided by the LANL Institutional Computing Program. This research also used re-

sources of NERSC with award numbers FES-ERCAP-m4239 and m4364.

Software: Athena++ (Stone et al. 2020), Matplotlib (Hunter 2007), Julia (Bezanson et al. 2017), MHDFlows (Ho 2022)

REFERENCES

- Armitage, P. J., Eisner, J. A., & Simon, J. B. 2016, *ApJL*, 828, L2, doi: [10.3847/2041-8205/828/1/L2](https://doi.org/10.3847/2041-8205/828/1/L2)
- Balbus, S. A., & Hawley, J. F. 1998, *Reviews of Modern Physics*, 70, 1, doi: [10.1103/RevModPhys.70.1](https://doi.org/10.1103/RevModPhys.70.1)
- Baronett, S. A., Yang, C.-C., & Zhu, Z. 2022, in *Bulletin of the American Astronomical Society*, Vol. 54, 102.381
- Bezanson, J., Edelman, A., Karpinski, S., & Shah, V. B. 2017, *SIAM Review*, 59, 65, doi: [10.1137/141000671](https://doi.org/10.1137/141000671)
- Birnstiel, T., Dullemond, C. P., & Brauer, F. 2010, *A&A*, 513, A79, doi: [10.1051/0004-6361/200913731](https://doi.org/10.1051/0004-6361/200913731)
- Birnstiel, T., Klahr, H., & Ercolano, B. 2012, *A&A*, 539, A148, doi: [10.1051/0004-6361/201118136](https://doi.org/10.1051/0004-6361/201118136)
- Brauer, F., Dullemond, C. P., & Henning, T. 2008, *A&A*, 480, 859, doi: [10.1051/0004-6361:20077759](https://doi.org/10.1051/0004-6361:20077759)
- Carrera, D., & Simon, J. 2022, in *Bulletin of the American Astronomical Society*, Vol. 54, 405.02
- Chen, K., & Lin, M.-K. 2020, *ApJ*, 891, 132, doi: [10.3847/1538-4357/ab76ca](https://doi.org/10.3847/1538-4357/ab76ca)
- Dominik, C., & Dullemond, C. P. 2024, *A&A*, 682, A144, doi: [10.1051/0004-6361/202347716](https://doi.org/10.1051/0004-6361/202347716)
- Drążkowska, J., & Dullemond, C. P. 2014, *A&A*, 572, A78, doi: [10.1051/0004-6361/201424809](https://doi.org/10.1051/0004-6361/201424809)
- Drążkowska, J., Li, S., Birnstiel, T., Stammler, S. M., & Li, H. 2019, *ApJ*, 885, 91, doi: [10.3847/1538-4357/ab46b7](https://doi.org/10.3847/1538-4357/ab46b7)
- Dubrulle, B., Morfill, G., & Sterzik, M. 1995, *Icarus*, 114, 237, doi: [10.1006/icar.1995.1058](https://doi.org/10.1006/icar.1995.1058)
- Estrada, P. R., Cuzzi, J. N., & Morgan, D. A. 2016, *ApJ*, 818, 200, doi: [10.3847/0004-637X/818/2/200](https://doi.org/10.3847/0004-637X/818/2/200)
- Estrada, P. R., Cuzzi, J. N., & Umurhan, O. M. 2022, *ApJ*, 936, 42, doi: [10.3847/1538-4357/ac7ffd](https://doi.org/10.3847/1538-4357/ac7ffd)
- Garate, M., Birnstiel, T., Drązkowska, J., & Stammler, S. M. 2020, *A&A*, 635, A149, doi: [10.1051/0004-6361/201936067](https://doi.org/10.1051/0004-6361/201936067)
- Ho, K. W. 2022, *MHDFlows.jl*, v.0.2.1b, Zenodo, doi: [10.5281/zenodo.8242702](https://doi.org/10.5281/zenodo.8242702)
- Huang, P., & Bai, X.-N. 2022, *ApJS*, 262, 11, doi: [10.3847/1538-4365/ac76cb](https://doi.org/10.3847/1538-4365/ac76cb)
- Hunter, J. D. 2007, *Computing in Science and Engineering*, 9, 90, doi: [10.1109/MCSE.2007.55](https://doi.org/10.1109/MCSE.2007.55)
- Johansen, A., & Youdin, A. 2007, *ApJ*, 662, 627, doi: [10.1086/516730](https://doi.org/10.1086/516730)
- Kowalik, K., Hanasz, M., Wółtański, D., & Gawryszczak, A. 2013, *MNRAS*, 434, 1460, doi: [10.1093/mnras/stt1104](https://doi.org/10.1093/mnras/stt1104)
- Laibe, G., Gonzalez, J.-F., Maddison, S. T., & Crespe, E. 2014, *MNRAS*, 437, 3055, doi: [10.1093/mnras/stt1929](https://doi.org/10.1093/mnras/stt1929)
- Laune, J., Li, H., Li, S., et al. 2020, *ApJL*, 889, L8, doi: [10.3847/2041-8213/ab65c6](https://doi.org/10.3847/2041-8213/ab65c6)
- Li, R., & Youdin, A. N. 2021, *ApJ*, 919, 107, doi: [10.3847/1538-4357/ac0e9f](https://doi.org/10.3847/1538-4357/ac0e9f)
- Li, Y.-P., Li, H., Li, S., et al. 2020, *ApJL*, 892, L19, doi: [10.3847/2041-8213/ab7fb2](https://doi.org/10.3847/2041-8213/ab7fb2)
- Li, Y.-P., Li, H., Li, S., & Lin, D. N. C. 2019, *ApJ*, 886, 62, doi: [10.3847/1538-4357/ab4bc8](https://doi.org/10.3847/1538-4357/ab4bc8)
- McNally, C. P., Lovascio, F., & Paardekooper, S.-J. 2021, *MNRAS*, 502, 1469, doi: [10.1093/mnras/stab112](https://doi.org/10.1093/mnras/stab112)
- National Academies of Sciences, Engineering, and Medicine. 2022, *Origins, Worlds, and Life: A Decadal Strategy for Planetary Science and Astrobiology 2023-2032* (Washington, DC: The National Academies Press), doi: [10.17226/26522](https://doi.org/10.17226/26522)
- Rucska, J. J., & Wadsley, J. W. 2023, *MNRAS*, 526, 1757, doi: [10.1093/mnras/stad2855](https://doi.org/10.1093/mnras/stad2855)
- Schaffer, N., Yang, C.-C., & Johansen, A. 2018, *A&A*, 618, A75, doi: [10.1051/0004-6361/201832783](https://doi.org/10.1051/0004-6361/201832783)
- Sengupta, D., & Umurhan, O. M. 2023, *ApJ*, 942, 74, doi: [10.3847/1538-4357/ac9411](https://doi.org/10.3847/1538-4357/ac9411)
- Stone, J. M., Tomida, K., White, C. J., & Felker, K. G. 2020, *ApJS*, 249, 4, doi: [10.3847/1538-4365/ab929b](https://doi.org/10.3847/1538-4365/ab929b)
- Tominaga, R. T., & Tanaka, H. 2023, *ApJ*, 958, 168, doi: [10.3847/1538-4357/ad002e](https://doi.org/10.3847/1538-4357/ad002e)
- Umurhan, O. M., Estrada, P. R., & Cuzzi, J. N. 2020, *ApJ*, 895, 4, doi: [10.3847/1538-4357/ab899d](https://doi.org/10.3847/1538-4357/ab899d)
- Wurm, G., & Teiser, J. 2021, *Nature Reviews Physics*, 3, 405, doi: [10.1038/s42254-021-00312-7](https://doi.org/10.1038/s42254-021-00312-7)
- Yap, T. E., & Batygin, K. 2024, *Icarus*, 417, 116085, doi: [10.1016/j.icarus.2024.116085](https://doi.org/10.1016/j.icarus.2024.116085)
- Youdin, A. N. 2010, in *EAS Publications Series*, Vol. 41, *EAS Publications Series*, ed. T. Montmerle, D. Ehrenreich, & A. M. Lagrange, 187–207, doi: [10.1051/eas/1041016](https://doi.org/10.1051/eas/1041016)
- Youdin, A. N., & Goodman, J. 2005, *ApJ*, 620, 459, doi: [10.1086/426895](https://doi.org/10.1086/426895)
- Zhu, Z., & Yang, C.-C. 2021, *MNRAS*, 501, 467, doi: [10.1093/mnras/staa3628](https://doi.org/10.1093/mnras/staa3628)